Microstructural Changes in Ni-YSZ Electrodes Operated in Fuel Cell and Electrolysis Modes: Effect of Gas Diffusion Limitations

D. M. Cox, S. A. Barnett

Department of Materials Science and Engineering, Northwestern University, Evanston, Illinois 60208, USA

Ni-YSZ electrode support symmetric cells were operated at 0, 0.75, 1.00, and 1.50 A/cm² for 1000 h in 50% H₂-50% H₂O at 800 °C. Electrochemical fracture at the anode-electrolyte interface is observed to occur under high anodic overpotential. Ni migration is observed and quantified over time at the anode of the polarized cells; however, the cathode shows no migration compared to control. Gas diffusion calculations show that steam is significantly enriched and depleted at the anode and cathode respectively, leading to the formation or suppression of volatile Ni(OH)_x species, which have been hypothesized as a transport pathway for Ni. However, gas flux calculations show that chemical evaporation alone is unlikely to be fast enough to induce the Ni loss observed.

Introduction

Ni-YSZ cermet composite electrodes remain the dominant architecture for electrode-supported solid oxide cells (SOC), both in anodic (fuel cell) and cathodic (electrolysis) operation. The composite electrode is inexpensive, high performing when the microstructure is properly engineered, and easy to manufacture with existing ceramic processing. Because the electrodes are manufactured as composite of NiO-YSZ followed by reduction to cermet Ni-YSZ, the Ni is far from an equilibrium distribution initially. This makes the electrode prone to degradation at the high operating temperatures employed (700 - 850 °C) due to microstructural redistribution of the Ni. This redistribution decreases the three-phase boundary (TPB) density, the location of all electrochemical reactions, and leads to susceptibility to redoxidation-initiated fracture due to the expansion of Ni to NiO.

Under no current flow through the electrode, Ni redistribution has no biased direction; Ni particles coarsen by surface diffusion or evaporation-condensation to minimize the surface energy^{1,2}. At the macrohomogeneous electrode level, the electrode can be reduced to a 1D system wherein the electrochemical potentials of each of the principal species vary as a function of distance from the electrolyte. Polarization, then, adds bias to the process of Ni redistribution, which has been observed by many researchers and termed "Ni migration."

While Ni migration has been observed, the underlying cause has not yet been determined. This is, in part, due to seemingly incongruous results between researchers, where Table I summarizes reports of Ni migration, the direction of Ni redistribution with respect to the electrolyte, and the operation mode tested. Mogensen's theory is the most widely accepted attempt to unify these results: Ni forms Ni(OH)_x species, which diffuse

either by surface diffusion or evaporation-condensation of the more volatile species. The expectation is that at higher temperatures, as was the case in Hauch (950 °C), the vapor pressure of Ni(OH)_x is higher and leads to increased kinetics of the evaporation-condensation process ^{2,3}. At lower temperatures the surface diffusion process is dominant, with the higher steam content associated with electrolysis leading to high coverage of Ni(OH) adsorbate which is known to be the fast-diffusing surface species ^{2,4}. This would also explain why the condition is more severe at electrolyzer stack inlet than outlets; at the latter steam content has been greatly diminished.

TABLE I. A brief summary of the direction of Ni migration observed in literature.

<u>`</u>		
Operation Mode	Ni Migration Direction	Source
Fuel Cell	Towards Electrolyte	5
	Away from Electrolyte	This work
Electrolyzer	Towards Electrolyte	3
•	Away from Electrolyte	2,6,7
	Stable	This work, 8

Here we use a method developed by Cox that uses laser-scribed Ni-YSZ electrode-supported symmetric cells (ESSC) to study polarization-induced microstructural evolution by periodic sampling the microstructure over time while maintaining an accurately controlled cell area ⁹. The ESSCs enable rapid screening by parallel or in-series operation in the same environmental chamber, simultaneous anodic (fuel cell) and cathodic (electrolyzer) polarization of Ni-YSZ, and the elimination of seals, but the simultaneous operation of the two electrodes requires that both electrodes stably operate in a given gas condition, making high steam operation difficult without oxidation of Ni in the anode.

The four ESSCs were operated at 800 $^{\circ}$ C in a 50% $\rm H_2$ 50% $\rm H_2O$ gas environment, where both anodic and cathodic operation are relevant. Cells 1-4 are operated at current densities (j) of 0, 0.75, 1.00, and 1.50 A/cm², and all display stable cathodic operation, contrary to many reports in these conditions, but great performance degradation and failure at the anode due to Ni depletion and electrochemical fracture. This is explained by gas diffusion limitations within the support, which cause steam enrichment at the anode and depletion at the cathode.

Methods

ESSCs were produced by tape casting, lamination, and co-sintering as described elsewhere ⁹. ESSCs were then reduced and laser-scribed ⁹, producing samples with 4 discrete removable sections (see insets in Figure 1) that can be analyzed during the life test. Samples were cut into 1.0, 0.75, and 0.5 cm² squares to create different current densities with a single current source. Microstructural sampling required a thermal cycle to ambient temperature by decreasing the furnace temperature to room temperature at 1 °C/min, hand fracturing off a segment (accounting for 1/8 of the initial active area) and ramping the furnace back to operating T at the same rate. After segment removal, the current was adjusted to maintain the same current density.

Electrochemical testing of the samples was performed using a SquidStat Pro (Admiral Instruments). Cells were operated galvanostatically at j = 0, 0.75, 1.00, or 1.50 A/cm^2 . Only

total voltage across all cells was measured in real time, so galvanostatic holds for 2 minutes were taken with every 1 - 2 days to estimate the total voltage of each cell during operation.

Microstructural sampling was performed at 100, 500, and 1000 h. 2D analysis was performed with a JEOL-7900 FLV SEM. The porous samples were vacuum infiltrated with Buehler Epothin II and mechanically polished to 50 nm. Low-voltage secondary electron (LVSE) imaging was used to determine Ni connectivity according to Thyden's procedure ¹⁰, and a dedicated backscatter electron (BSE) detector was used to determine porosity. 3D microstructural analysis was collected using a Helios Nanolab FIB-SEM (FEI) by serial sectioning to inform transport properties of the electrodes. 3D data was smoothed by a non-local means algorithm ¹¹ segmented by a two-step segmentation process implemented using python with sci-kit image ¹²: pre-segmentation using Otsu's method followed by watershed segmentation. Tortuosity of the pore phase was measured using TauFactor which directly calculates the attenuation in flux through the 3D structure at steady-state compared to a control volume of the same dimensions ¹³.

To test the hypothesis that mass-transport-induced changes in steam/hydrogen content helps determine Ni migration, a detailed analysis of gas diffusion was carried out. At high temperature and small pore size, the diffusivity of the support must consider both binary diffusivity (D_{ij}) and Knudsen diffusivity ($D_{Kn,i}$), defined elsewhere ¹⁴. The two diffusivities overlap in their pathway, so it is common to add their reciprocals in what is called the Bosanquet formula.

$$D_i = \frac{D_{ij}D_{Kn,i}}{D_{ij} + D_{Kn,i}} \tag{1}$$

The effective diffusivity of species *i* through a macrohomogeneous porous cermet composite is then

$$D_{cermet,i}^{eff} = \frac{\epsilon}{\tau} D_{cermet,i}$$
 [2]

Where ϵ is the porosity and τ is the tortuosity factor of the gas phase. To account for the effects of large non-overlapping pore formers distributed throughout the electrode support, a diffusivity term was developed according to Crank ¹⁵. Under the assumptions that the large pores are randomly distributed and the unimpeded binary diffusivity in the large pores is much greater than D_{cermet}^{eff} , a multiplication factor can be applied to D_{cermet}^{eff} to determine the diffusivity of the support, D_S .

$$\left(1 + \frac{A_A^2}{1 - A_A}\right) \le \frac{D_{S,i}}{D_{cermet,i}^{eff}} = M_D \le \left(1 + \frac{A_A}{1 - A_A}\right)$$
[3]

Where A_A is the area fraction of large pore in a cross sectional image of the support electrode ¹⁶. To solve for the partial pressures of H₂ and H₂O at the electrode-electrolyte interface, Fickian diffusion is assumed giving ¹⁷:

$$P_i^{active} = P_i^{inlet} + \frac{RT}{nF} \frac{L_S}{D_{S,i}} j = P_i^{inlet} \left(1 + \frac{j}{j_{lim,i}} \right)$$
 [4]

 L_s is the thickness of the electrode, n is the number of electrons in the reaction (2), and $j_{lim,i}$ is the limiting current density of component i. Here, j is defined as positive for cathodic polarization and negative for anodic polarization, so j_{lim,H_2} is negative and j_{lim,H_2} 0 is positive.

The vapor pressure of Ni(OH)_x species were calculated assuming first order reactions of the reaction $Ni(OH)_x(g) + \frac{x}{2}H_2(g) \rightleftharpoons Ni(s) + xH_2O(g)$, with the equilibrium constants derived from fitting Mogensen's reported data ².

Results

Electrochemical Measurements

Total voltage versus time for each polarized cell is shown in Figure 1. Cell 4, operating at the highest current density (1.5 A/cm²), operated at ~900 mV before failing at 100 h, necessitating a ramp down and removal. The remaining three cells were operated up to 1000 h. Cell 2 (0.75 A/cm²) increased from 450 to 600 mV over the first 100 h, then fluctuated around that value for the remaining 900 h. Cell 3 (1.0 A/cm²) increased steadily from 600 mV at 24 h to 900 mV at 700 h before rapidly increasing up to 1400 mV at 850 h, after which voltage during galvanostatic holds was unstable.

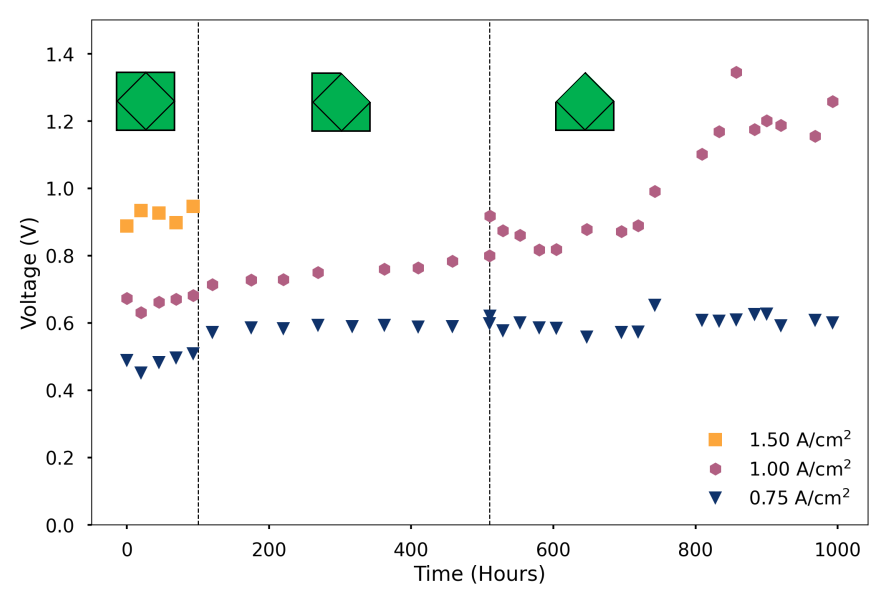


Figure 1: Operating voltages of Cells 2-4 versus time. Dotted lines mark the points of microstructure sampling, and diagrams show portion of ESSCs remaining at a given stage in the life test.

Microstructural Observations

The failures of Cell 4 (at 100 h) and Cell 3 (at 833 h) were both found to be via similar fracture along the anode-electrolyte interface. In both cases, a large voltage increase was observed in galvanostatic measurements prior to failure. Figure 2 shows cross sectional SEM images of the two parts of cell 4 after failure, the cathode and electrolyte (2a) and the

anode (2b). Both the YSZ electrolyte and the Ni-YSZ electrode appear to be completely intact with no obvious damage; instead, the fracture is a clean cleave at the interface. This could be explained by reoxidation of Ni; however, calculations of steam content at the electrode show much a much lower $H_2O:H_2$ ratio than necessary to chemically reoxidize (~100:1) ¹⁸, and the fracture here is different than in prior reports of Ni-YSZ reoxidation where periodic cracks formed normal to the electrolyte and within the electrode ¹⁹.

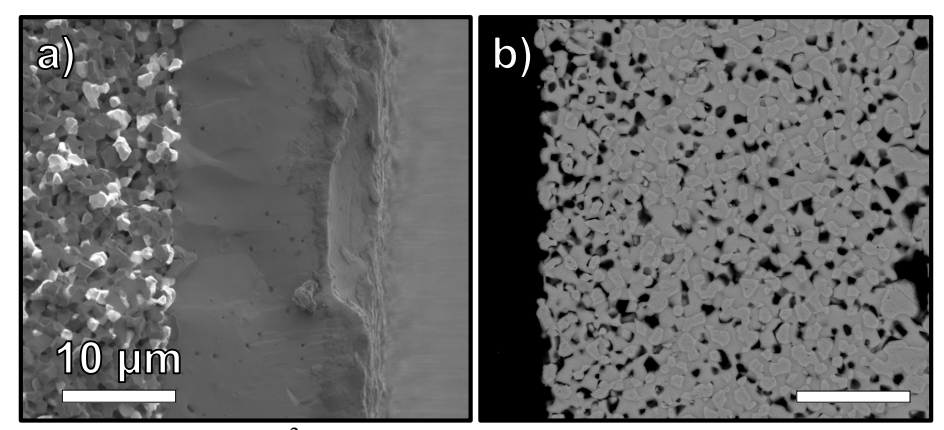


Figure 2: Cell 4 ($j = 1.50 \text{ A/cm}^2$) fractures along the anode-electrolyte interface under high voltage. a) Cathode and electrolyte as a fractured cross section show no failures at their interface, nor damage to the electrolyte. No pieces of anode are visible. b) BSE image of anode infiltrated with epoxy. No electrolyte is attached, implying clean fracture at the interface.

Figure 3 shows Cell 3 through time using both BSE (a-c) and LVSE (d-f) imaging, along with corresponding area fraction of the pore and percolated Ni phases as a function of distance from the cathode-electrolyte interface (g-i). No Ni depletion was observed at the cathode of any cells regardless of current density, contrary to reports for cells tested for similar times at these current densities and temperature ^{6,7}. Rather, severe Ni depletion and deactivation was observed at the anode at high current density. In addition to Ni depletion, the Ni that remains in the depletion region has a faint grey contrast that under these imaging conditions indicates that it is almost entirely electrically isolated. The depletion regions were measured to be ~ 0 , 5, and 10 μ m at 100, 500, and 1000 h respectively. No evidence of local Ni enrichment near the depleted region was found, which would correspond to a local lower than average porosity in g-h, this observed net Ni loss in the electrode would be unlikely to occur under a surface diffusion pathway due to its short range. Evaporationcondensation pathways, instead, could transport Ni from the active electrode into the bulk support where particle size is much larger, such that Ni enrichment would be difficult to detect. Thus, the results in Figure 3 are more consistent with an evaporation-condensation pathway.

Figure 4 shows Cells 1, 2, and 3 at 1000 h, showing that increasing the current density also increases the rate of Ni loss. It also shows no clear difference in the cathodes after 1000 h of annealing (Cell 1) or operation (Cells 2 and 3). The depletion region for Cell 2 at 1000 h is \sim 4 µm, showing that the rate of depletion is \sim 40% that of Cell 3.

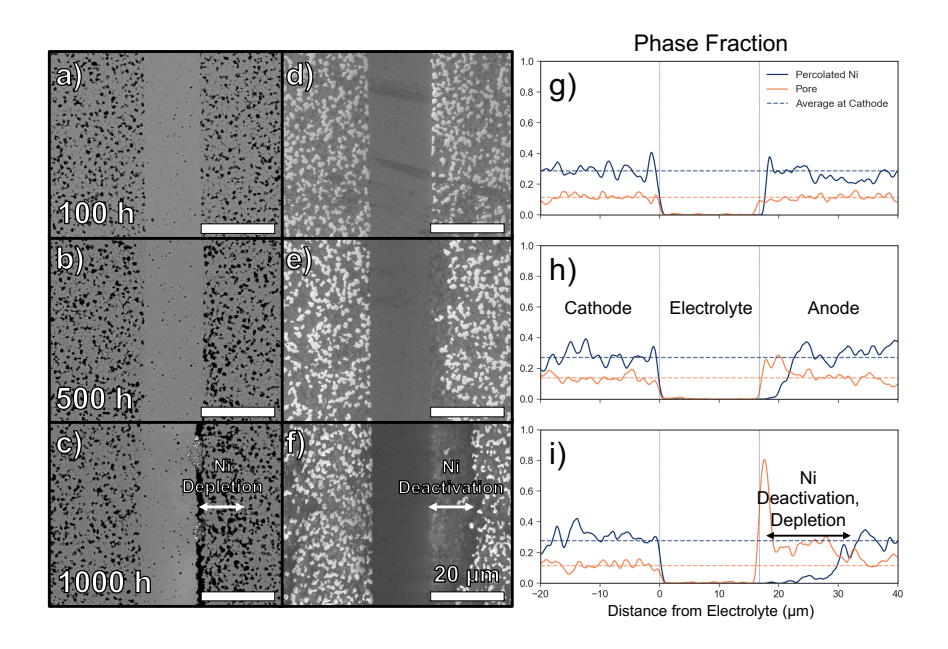


Figure 3: BSE (a,b,c), and LVSE (d,e,f) imaging at 100, 500, and 1000 h of the cell life tested at 1.0 A/cm². The depletion region and deactivation region in each show perfect overlap. The average pore and percolated Ni fraction at the cathode show low deviation, and at the anode away from the depletion region, the structure appears identical to the cathode.

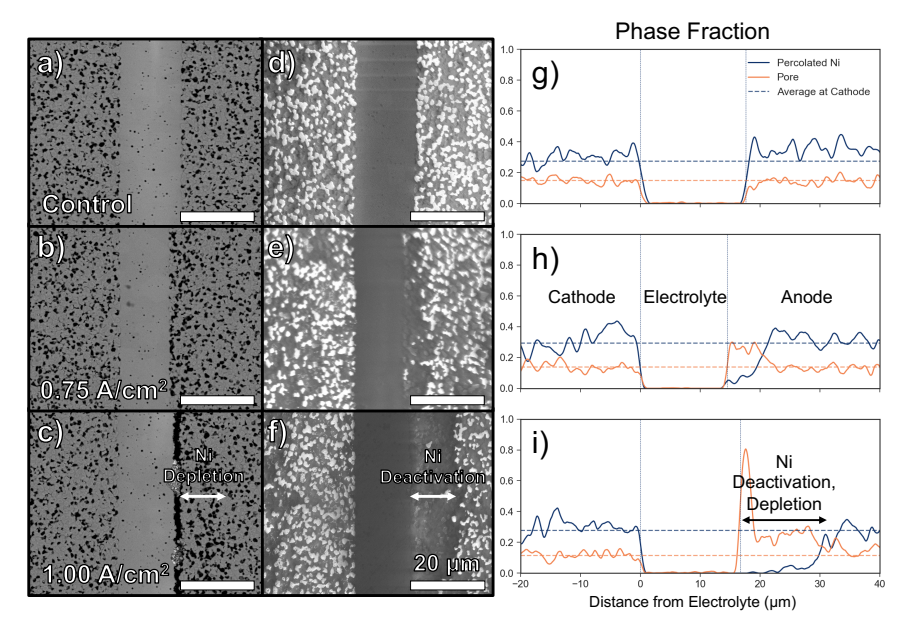


Figure 4: Comparison of Cells 1, 2, and 3 (0, 0.75, 1.00 A/cm²) that were tested up to 1000 h. Increasing the current density causes a clear increase in Ni loss at the anode, but no detectable change at the cathode, compared to Cell 1.

Diffusion Analysis

2D and 3D analysis of Cell 1 at 500 h was used to obtain a baseline microstructure representing all the cell functional layers in the calculations. They generated values of $L_s = 150 \,\mu m$, $M_D = 1.05 - 1.25$, $\epsilon = 0.16$ and $\tau = 44$, the last term generating the most

significant gas transport limitations. ϵ is smaller than the theoretical porosity (0.175) because only non-isolated pores are considered, and τ is large due to the presence of many dead-end pores that do not assist with gas flow. Plugging these into Eq. 3 using the average value for M_D gives $D_{S,H_2O} = 0.019$ cm²/s and $D_{S,H_2} = 0.049$ cm²/s, which are in line with EIS measurements of cells produced by the same conditions in low steam conditions by Cox ⁹ where $D_{S,H_2O} = 0.015 - 0.02$ cm²/s. Plugging these values into Eq. 4 gives $j_{lim,H_2O} = 1.37$ A/cm² and $j_{lim,H_2} = -3.52$ A/cm², which are consistent with values from literature ²⁰.

The gas partial pressures at the electrode-electrolyte interface P_i are shown in Table II. The results show clear and significant altering of the gas composition at the electrode-electrolyte interface compared to the inlet, particularly in P_{H_2O} due to the asymmetric effects of Knudsen diffusion. The calculations result in a non-physical negative pressure value for Cell 4 at the cathode; however, these calculations do not consider the effects of convection or electronic conductivity in YSZ under reducing conditions that could enable this cell to operate.

TABLE II. Calculated gas partial pressure at the electrode-electrolyte interface.

Electrode	Gas Species	$j = 0.75 \text{ A/cm}^2$	$j = 1.00 \text{ A/cm}^2$	$j = 1.50 \text{ A/cm}^2$
Anode	P_{H_2}	0.39 atm	0.36 atm	0.29 atm
	P_{H_2O}	0.77 atm	0.87 atm	1.05 atm
Cathode	P_{H_2}	0.61 atm	0.64 atm	0.71 atm
	P_{H_2O}	0.23 atm	0.13 atm	-0.05 atm

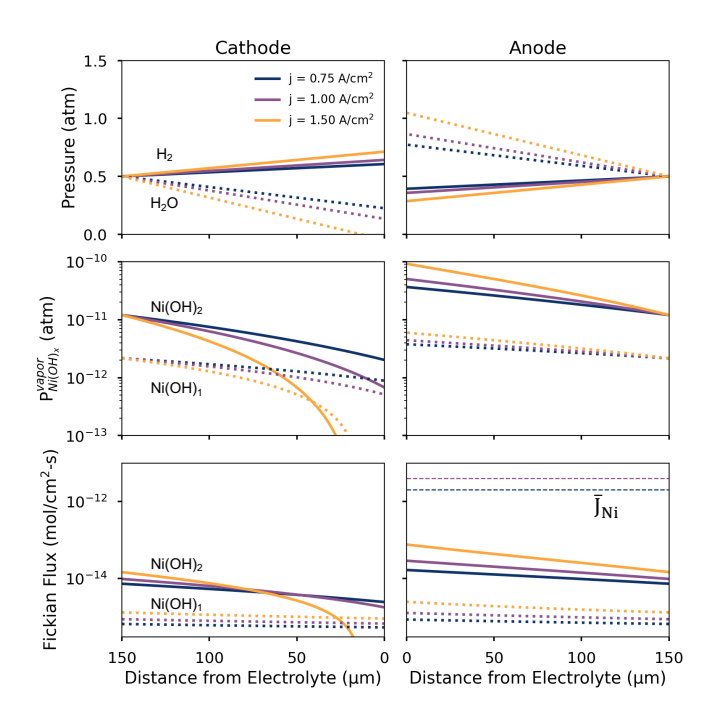


Figure 5: Calculated gas compositions based on microstructural analysis. P_{H_2O} at the anode-electrolyte interface is 10-100x higher than at the cathode, which leads to slower Ni vapor transport at the cathode compared to the anode. Ni(OH)₂ vapor pressure gradients fail to produce high enough flux from Fickian diffusion to explain the microstructural observations.

At steady-state, assuming all reactions occur at the electrode-electrolyte interface, P_i will vary linearly from the inlet to the interface, so gas composition throughout the electrode can be calculated, as shown in Figure 5. The vapor pressure of $P_{Ni(OH)_x}$ species can then be calculated as well, which show clear increase at the anode and decrease at the cathode. Assuming Fickian diffusion and that $D_{Kn,Ni}$ dominates the diffusivity term, the gas phase flux of Ni can be calculated using the same microstructural parameters as above. This can then be compared to the total flux of Ni from microstructural analysis where:

$$J_{Ni} = \frac{W_D V_D \rho_{Ni}}{M_{Ni} t} \tag{5}$$

Where W_D is the width of the depletion region, V_D is the fractional volume of the depleted region by fraction, ρ_{Ni} and M_{Ni} and the density and molar mass of Ni, respectively, and t is the total time passed.

Discussion

Fracture of Ni-YSZ Anodes

The present observed fracture parallel to the anode-electrolyte interface is inconsistent with literature examples of redox fracture 19. Furthermore, the calculated steam and hydrogen partial pressures are not close to the values where Ni oxidizes even at the higher current density. Additionally, the diffusivity of the support is not expected to change significantly over the lifetime of the experiments, so galvanostatic operation should not lead to increased steam content that can eventually chemically oxidize the Ni. Instead, electrochemically induced fracture is the likely cause, wherein Ni is oxidized directly by YSZ locally. Wagner showed that in the absence of available H₂, in anodic operation, YSZ will oxidize Ni directly forming a NiO interlayer between Ni and YSZ 21; their experiments grew up to 4 µm thick NiO layers between flat YSZ substrates and sputtered Ni electrodes. As the resistance of Cell 3 increases over time, so too will μ_{0_2} in YSZ at the anode, with the highest value at the interface. Local expansion from Ni oxidation would then create local stress along that interface. Closed pores could further exacerbate this effect by locally trapping steam to the point of Ni oxidation, but this effect would be small compared to electro-oxidation. The loss of Ni over time, in the case of Cell 3, would also decrease the electrode strength near the electrolyte, even if the Ni there is not electrochemically active. Under galvanostatic operation, once runaway voltage is reached, the process accelerates (around 800 h) and rapidly expands the affected Ni, leading to complete fracture.

Ni Depletion

Ni depletion at the anode is in line with Mogensen's theory of $Ni(OH)_x$ volatile species transporting Ni from the active electrode to the bulk 2 , with $Ni(OH)_2$ being 10 times as prevalent as Ni(OH); however, quantitative analysis of the gas diffusion fails to reach the required average flux to induce 10% total volume loss of Ni at the anode at 0.75 or 1.00 A/cm² over 1000 h. If gas species are the source of Ni depletion, Mogensen's value for vapor pressures must be too low, or another source must be increasing $Ni(OH)_x$. One option is that local curvature increases the vapor pressure due to the Gibbs-Thomson effect, but the particle sizes of Ni in this structure, ~500 nm radius, are too large to induce more than

a small increase in vapor pressure²². Electrowetting could cause a change in local curvature, thereby increasing the vapor pressure, but Jiao has definitively shown *in situ* that anodic potential *increases* wetting, thereby decreasing the curvature and vapor pressure ^{23,24}. Anodic overpotential, however, will lead to an increase in μ_{O_2} in YSZ, so if the oxidized Ni species Ni(OH)₂ is formed by an electrochemical pathway, then the vapor pressure could be many orders of magnitude higher than the chemical vapor pressure with even modest voltages. Another possibility is that the total differential pressure due to the asymmetric diffusion of H₂ and H₂O can force Ni(OH)₂ convection enough to result in this flux, but this is unlikely to result in a 100x increase in evaporation rate.

The stable cathode is likely caused by the gas transport limitations of the support. Because the cathode and anode microstructures are identical, there is no inherent stability of the active electrode. If Ni migrates via Ni(OH)_x species either as surface adsorbate or gas, suppression of steam at the cathode will directly lead to suppression of these species, which will in turn decrease the rate of migration. The effects of support structures then are significant and could explain differences between groups that use different support microstructures, wherein some report no Ni migration during electrolysis. More importantly, this could provide an avenue for improving the stability of solid oxide electrolyzers.

Conclusions

There are two important differences between the present results and prior reports:

- 1. Although Ni depletion has been observed in Ni-YSZ anodes before, it normally occurs at a higher temperature (≥850 °C) than the present 800 °C value;
- 2. Cathodic Ni migration is not observed here, different than in several reports under the same conditions, 800 °C and 1.0 A/cm²

Both findings can in large part be explained by the effects of gas transport limitations, which are likely more pronounced in the present Ni-YSZ supports due to the relatively low porosity and high tortuosity. Because Ni(OH)₂ species are dependent both on local P_{H_2O} and local P_{H_2} , enrichment of steam at the anode will enable significantly higher hydroxide vapor pressure. If considering an electrochemical pathway, the effects would be even more pronounced. It then follows that depletion of steam at the cathode is responsible for the lack of Ni migration. The design of the Ni-YSZ support microstructure is thus a tool that can potentially be used to control Ni migration.

Acknowledgments

The authors gratefully acknowledge financial support by the US National Science Foundation (NSF DMR-1912530). This work made use of the NUFAB and EPIC facilities of Northwestern University's NUANCE Center, which has received support from the SHyNE Resource (NSF ECCS-2025633), the IIN, and Northwestern's MRSEC program (NSF DMR-1720139). This work also made use of the Materials Characterization and Imaging Facility which receives support from the MRSEC Program (NSF DMR-1720139) of the Materials Research Center at Northwestern University.

References

- 1. H.-Y. Chen, H.-C. Yu, J. Scott Cronin, J. R. Wilson, S. A. Barnett, and K. Thornton, *J. Power Sources*, **196**, 1333–1337 (2011)
- 2. M. B. Mogensen, M. Chen, H. L. Frandsen, C. Graves, A. Hauch, P. V. Hendriksen, T. Jacobsen, S. H. Jensen, T. L. Skafte, and X. Sun, *Fuel Cells*, **21**, 415–429 (2021).
- 3. A. Hauch, S. D. Ebbesen, S. H. Jensen, and M. Mogensen, *J. Electrochem. Soc.*, **155**, B1184 (2008)
- 4. J. Sehested, N. W. Larsen, H. Falsig, and B. Hinnemann, *Catal. Today*, **228**, 22–31 (2014).
- 5. N. H. Menzler, D. Sebold, Y. J. Sohn, and S. Zischke, J. Power Sources, 478 (2020).
- 6. F. Monaco, M. Hubert, J. Vulliet, J. P. Ouweltjes, D. Montinaro, P. Cloetens, P. Piccardo,
- F. Lefebvre-Joud, and J. Laurencin, J. Electrochem. Soc., 166, F1229–F1242 (2019)
- 7. M. Trini, A. Hauch, S. De Angelis, X. Tong, P. V. Hendriksen, and M. Chen, *J. Power Sources*, **450** (2020).
- 8. O. A. Marina and M. Tucker, *H2NEW: Hydrogen (H2) from Next-generation Electrolyzers of Water HTE: Durability and AST Development*, (2021).
- 9. D. M. Cox and S. A. Barnett, *J. Electrochem. Soc.*, **170**, 024514 (2023) https://iopscience.iop.org/article/10.1149/1945-7111/acbb30.
- 10. K. Thydén, Y. L. Liu, and J. B. Bilde-Sørensen, *Solid State Ionics*, **178**, 1984–1989 (2008).
- 11. J. Roels, F. Vernaillen, A. Kremer, A. Gonçalves, J. Aelterman, H. Q. Luong, B. Goossens, W. Philips, S. Lippens, and Y. Saeys, *Nat. Commun.* (2020)
- 12. S. van der Walt, J. L. Schönberger, J. Nunez-Iglesias, F. Boulogne, J. D. Warner, N. Yager, E. Gouillart, and T. Yu, S. Gomez, Editor. *PeerJ*, **2**, e453 (2014) https://doi.org/10.7717/peerj.453.
- 13. S. J. Cooper, A. Bertei, P. R. Shearing, J. A. Kilner, and N. P. Brandon, *SoftwareX*, **5**, 203–210 (2016).
- 14. S. K. Das, Chem. Eng. Sci., 203, 293–301 (2019).
- 15. J. Crank, *The Mathematics of Diffusion*, 2nd ed., p. 270–285, Oxford University PRess, (1976).
- 16. C. V Howard and M. G. Reed, *Unbiased Stereology: Three-Dimensional Measurement in Microscopy*, p. 94–95, (1999).
- 17. R. O'Hayre, S.-W. Cha, W. G. Colella, and F. B. Prinz, (2016).
- 18. J. Malcolm W. Chase, *NIST-JANAF thermochemical tables*, Fourth edition. Washington, DC: American Chemical Society; New York: American Institute of Physics for the National Institute of Standards and Technology, 1998., (1998)
- 19. A. Faes, A. Nakajo, A. Hessler-Wyser, D. Dubois, A. Brisse, S. Modena, and J. Van herle, *J. Power Sources*, **193**, 55–64 (2009).
- 20. B.-K. Park, R. Scipioni, Q. Zhang, D. Cox, P. W. Voorhees, and S. A. Barnett, *J. Mater. Chem. A* (2020).
- 21. T. Wagner, R. Kirchheim, and M. Rühle, Acta Metall. Mater., 40 (1992).
- 22. P. Munnik, M. E. Z Velthoen, P. E. de Jongh, K. P. de Jong, C. J. Gommes, P. Munnik,
- M. E. Z Velthoen, P. E. de Jongh, K. P. de Jong, and C. J. Gommes, *Angew. Chemie*, **126**, 9647–9651 (2014) https://onlinelibrary.wiley.com/doi/full/10.1002/ange.201404103.
- 23. J. Van herle, M. Cantoni, L. Navratilova, G. Jeanmonod, P. Caliandro, G. Rinaldi, and A. Nakajo, *J. Electrochem. Energy Convers. Storage*, **17** (2020).
- 24. Z. Jiao, N. Shikazono, and N. Kasagi, J. Power Sources, 196, 8366–8376 (2011).